Fracture properties of nickel-based anodes for solid oxide fuel cells

S. Goutianos [a,*], H.L. Frandsen [b], B.F. Sørensen [a]

[a] *Materials Research Division, Risø National Laboratory for Sustainable Energy, Technical University of Denmark, DK-4000 Roskilde, Denmark*
[b] *Fuel Cells and Solid State Chemistry Division, Risø National Laboratory for Sustainable Energy, Technical University of Denmark, DK-4000 Roskilde, Denmark*

Abstract

Reliable assessment of structural integrity of fuel cells requires the knowledge of the mechanical properties of their individual components, in particular the fracture toughness. A technique is presented to measure the critical energy-release rate/fracture toughness of thin ceramic layers such as the anode material (NiO–YSZ) in a fuel cell. The approach involves a new specimen geometry which consists of a thin ceramic glued onto thick steel beams to form a double cantilever beam (DCB) specimen. The fracture toughness values, measured from truly sharp cracks, are obtained over a range of applied energy-release rates: from crack growth initiation to fast fracture. The fracture toughness is measured to be $1.97 \pm 0.13\,\mathrm{MPa}\sqrt{m}$ at crack growth initiation.

© 2010 Elsevier Ltd. All rights reserved.

Keywords: Fracture energy; Stress intensity; Anode; Fuel cells

1. Introduction

Porous NiO–YSZ (nickel oxide in yttria stabilized zirconia) cermet is usually being used as anode material for solid oxide fuel cells (SOFC) applications[1,2] because of its relative low cost, catalytic properties and chemical stability. Its thermal expansion coefficient is also close to the YSZ electrolyte commonly used in SOFCs leading to relative low thermally induced residual stresses. As SOFCs are electrochemical devices that convert chemical energy into electrical energy, extensive work has been performed towards optimisation of anode microstructure to tailor its electrochemical performance, see *e.g.* Primdhal and Mogensen.[3,4] On the other hand limited work has been reported on the mechanical properties and in particular the fracture toughness of the anode material[5–8] and the other SOFC components. This lack of mechanical data is a drawback when designing an SOFC stack as it has to withstand high stresses, arising mainly from a mismatch in thermal expansion coefficients of the different ceramic layers and thermal gradients, during operation.[9] Among the various mechanical properties, the fracture toughness (critical Mode I stress intensity factor, K_{Ic}) or fracture energy (critical Mode I energy release rate, $\mathcal{G}_{Ic}$) values are of particular importance to assess the structural integrity of ceramic (brittle) materials such as NiO–YSZ or Ni–YSZ.

As already mentioned, data concerning the fracture properties of the anode material are limited. Radovic and Lara-Curzio[6] recently reported the fracture toughness of NiO–YSZ and Ni–YSZ as a function of porosity using the double torsion (DT) test, whereas Hbaieb[7] used the controlled buckling test developed by Chen et al.[10] Here, the fracture toughness and fracture energy are measured using the double cantilever beam (DCB) test. Since the effect of the porosity on fast fracture (explained below) is clearly demonstrated by Radovic and Lara-Curzio[6] on both NiO–YSZ and Ni–YSZ, in the present paper we limit ourselves only in studying the fracture behaviour of NiO–YSZ of a certain porosity and certain grain sizes for the NiO and YSZ phases.

The focus is (a) on developing a test method which is particular suited for testing of thin solid films enabling testing of materials processed in the same way as real components and (b) examining in detail the crack growth in NiO–YSZ over a range of applied energy release rates as it is well established that the fracture toughness of brittle materials can depend on crack velocity, v.[11–13] The applied energy release rate, $\mathcal{G}$, causing fast fracture (the crack grows at a velocity about a third of the speed of sound) is denoted by $\mathcal{G}_{Ic}^{f}$. Brittle materials can fail,

* Corresponding author. Tel.: +45 4677 5823; fax: +45 4677 5758.
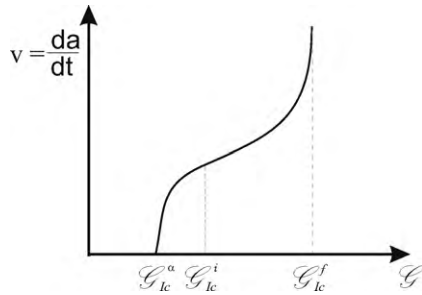*E-mail address:* gout@risoe.dtu.dk (S. Goutianos).

Fig. 1. The variation of crack-growth velocity as a function of the applied energy release rate. $\mathcal{G}^i_{Ic}$, $\mathcal{G}^f_{Ic}$, and $\mathcal{G}^a_{Ic}$ indicate the initiation of crack growth, fast fracture, and crack arrest of a sharp crack, respectively.

Fig. 2. Double cantilever beam (DCB) specimen loaded with pure bending moments.

Table 1
Material properties.

	Young's modulus (GPa)	Poisson's ratio
NiO–YSZ	155	0.23
Steel	200	0.30

however, at applied energy release rates much lower than the one causing fast fracture (see Fig. 1). In this case, the crack growth takes place at lower velocities; this phenomenon is called sub-critical crack growth. Knowledge of the relationship between the resulting crack growth velocity and energy release rate is important to prevent failure in materials that exhibit subcritical crack growth behaviour. Safe design should be based on $\mathcal{G}$ values that correspond to crack arrest and not fast fracture. The critical energy release rate is denoted as $\mathcal{G}^a_{Ic}$ (see Fig. 1). The energy release rate necessary to cause crack initiation from a stationary sharp crack is $\mathcal{G}^i_{Ic}$ and can be different from $\mathcal{G}^a_{Ic}$ [9] as shown schematically in Fig. 1. A sharp precrack is essential for accurate evaluation of the critical energy release rate $\mathcal{G}_{Ic}$. Numerous studies have shown that if a saw-cut notch is used instead of a sharp crack, then the measured toughness value increases with increasing the notch root radius, e.g. Nishida et al.[14], Damani et al. [15], and Sherman.[16]

It is, therefore, indented in this work to describe a test method, which involves simple specimen geometries, suited to accurate determination of $\mathcal{G}$–v relationships (Fig. 1) for brittle materials such as porous NiO–YSZ.

2. Analysis

The analysis of the DCB specimen loaded with pure bending moments is based on the specimen configuration shown in Fig. 2. It consists of a thin NiO–YSZ layer glued inside the grooves of
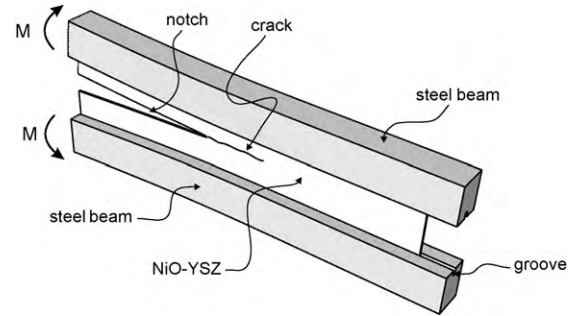
two steel beams that are mounted on special fixture (described in the next section), which applies pure bending moments.[17] This specimen is a steady-state configuration, because under constant moment, $\mathcal{G}$ is independent of the crack length.[17] Measurement of the applied moment suffices to calculate $\mathcal{G}$.

The energy release rate is analysed through the path independent J integral.[18] Before evaluating the J integral, the cross-section of the specimen (Fig. 3(a)) is transformed to an approximate equivalent cross-section of uniform width, B, as can be seen in Fig. 3(b). The equivalent cross-section has a Young's modulus, for the ceramic layer, equal to $E^*_1 = (b/B)E_1 = \xi E_1$ with $\xi = b/B$, where b is the width of the ceramic layer. This is an approximation, since the adhesive layer and part of the ceramic layer, material # 1 ($h_c - h$, see Fig. 3(a)) are replaced by steel (material #2).

The elastic properties, measured by uniaxial tension for the ceramic layer, are given in Table 1.

When evaluating the J integral along the external boundaries of the specimen (Fig. 4), the only non-zero contributions come from the beam ends. The beams are subjected to pure bend-
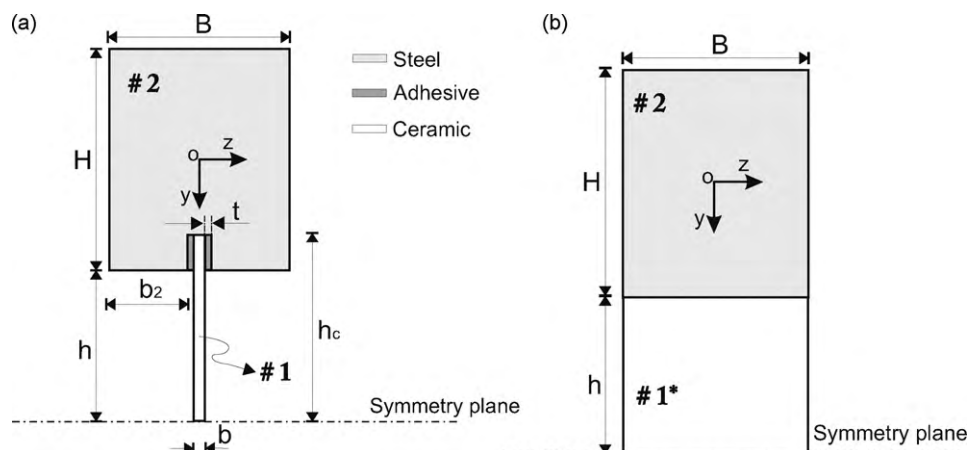

Fig. 3. Symmetric half specimen (a) cross-section, and (b) equivalent cross-section.

ing moments, and if the beams are few times longer than their height, the strain varies linearly across the height. Under these conditions, the J integral, for plane stress, is given by[19]:

$$J = \frac{1}{E_2} \frac{M^2}{B^2 h^3 I_o} \qquad (1)$$

where E_2 and ν_2 are the Young's modulus and Poisson's ratio of the steel beams, respectively, M is the applied moment and h is defined in Fig. 3. Eq. (1) is similar to the energy release rate formula for sandwich specimens of Bao et al.[19] The non-dimensional constant I_o, which differs from that of Bao et al.[19] due to the different widths of the two materials, depends on geometry and elastic constants:

$$I_o = \frac{1}{3}\left[\frac{1}{\eta^3} + \frac{3\Delta}{\eta}\left(\Delta - \frac{1}{\eta}\right) + \xi\bar{\Sigma}\left(1 + 3\left(\Delta - \frac{1}{\eta}\right)^2\right.\right.$$
$$\left.\left. -3\left(\Delta - \frac{1}{\eta}\right)\right)\right] \qquad (2)$$

where Δ is equal to:

$$\Delta = \frac{1 + 2\xi\eta\bar{\Sigma} + \xi\eta^2\bar{\Sigma}}{2\eta(\xi\eta\bar{\Sigma} + 1)} \qquad (3)$$

with $\eta = h/H$ and $\bar{\Sigma} = E_1/E_2$, where H is the height of the steel beams and E_1 is the Young's modulus of the ceramic layer. Finally, from the critical value of the J integral the critical energy release rate, $\mathcal{G}_{Ic}$, can be calculated, taking into account that the energy is released from the beams of width B, but energy is consumed by the fracture process over width b only:

$$J_{Ic}B = \mathcal{G}_{Ic}b \Rightarrow \mathcal{G}_{Ic} = J_{Ic}/\xi \qquad (4)$$

From $\mathcal{G}_{Ic}$, under elastic conditions, the critical plane stress Mode I stress intensity factor can be evaluated by[20]:

$$\mathcal{G}_{Ic} = \frac{K_{Ic}^2}{E_1} \qquad (5)$$

3. Experimental details

3.1. Materials and processing

The samples were prepared by mixing powders of NiO and 3 mol% Y_2O_3-stabilized ZrO_2 (3YSZ), which were processed into slurries. Thin foils were then made by tape casting and they were sintered at a temperature which resulted approximately
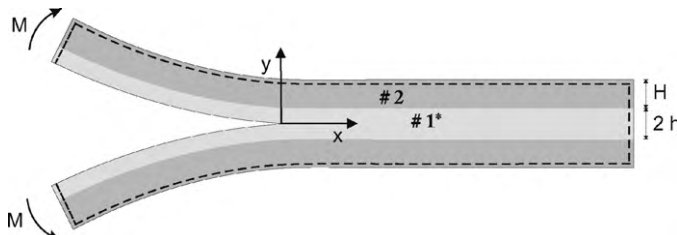
in 15 vol% porosity (measured by mercury porosimetry). The thickness of the specimens was approximately 0.3 mm.

3.2. Specimen geometry

Rectangular specimens with a central notch along the biggest dimension were laser cut from tape cast NiO–YSZ plates at dimensions approximately 10 mm × 60 mm × 0.3 mm. The notch length was 25 mm and the height 0.1 mm (notch radius = 50 μm). Fracture mechanics testing requires a sharp pre-crack, which is usually achieved by cyclic loading.[21] Fatigue precracking is quite difficult for thin ceramic layers as the ones used in the present work, and it is costly in general. Several approaches, therefore, have been proposed to precrack brittle materials for bending specimens[16,22–25] and compact-tension (CT) or DCB specimens.[26,27]

In the present work, two different ways to introduce a sharp crack at the root of the notch were tried. Following Kruzic et al.[27] the initial notch was sawed manually with a steel band that had its edge fine ground in the presence of 1 μm diamond slurry and simultaneously applying a pressure until a crack had "popped in". The disadvantage of this method was that since the crack introduced in a manual way, the introduced crack quite often propagated out of the mid-plane, and thus the specimen could not be used further. Specimen breakage also often occurred. Therefore, an additional micro-notch was sawed at the laser cut notch root with a steel blade. The result was a micro-notch with an approximate root radius less than 5–6 μm as can be seen in Fig. 5. It is known that even such a small notch can lead to erroneous toughness values. Here, the sawed micro-notch serves only to ensure that initial cracking takes place in the middle of the ceramic layer, as shown schematically in Fig. 2. Specimens without the micro-notch were also tested. In these cases, the initial crack growth led directly to catastrophic failure of the specimens. Details of the loading procedure are given below, whereas the fracture toughness values from the micro-notch are discussed in the next section.

The ceramic layer was then placed inside the grooves of two steel beams and glued using a two-part epoxy adhesive (Scotch-Weld[TM] DP460 from 3M) to form the test specimen—a double cantilever beam (DCB) specimen (Fig. 2). The height, H, of

Fig. 4. 2D specimen representation and J integral path along the external boundaries.
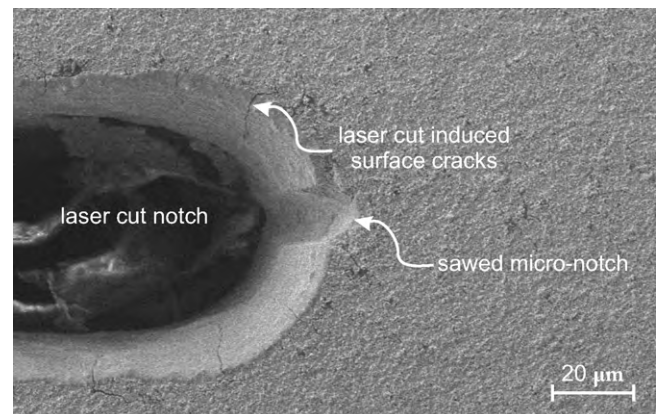

Fig. 5. Secondary-electron SEM micrograph of the final notch geometry.

the steel beams was 5.95 mm and the width, B, 4.85 mm (see Fig. 3(a)). The width of the ceramic layers, b, was approximately 0.3 mm and the half height was, h_c, 5 mm. The depth of the groove was 0.9 mm and thus $h = 4.1$ mm (see Fig. 3(a)). The width of the groove was 0.65 mm, and therefore the thickness of the adhesive layer, t (Fig. 3(a)), was approximately 0.175 mm. After some initial tests, it was found that the thickness of the adhesive layer, was difficult to control, but seemingly an important parameter. Initial experiments, without controlling the thickness uniformity, almost all resulted in crack kinking out of the mid-plane of the specimens and thus the experiments were invalid. In order to have a successful experiment, *i.e.* cracking along the middle of the ceramic layer without crack kinking towards the steel beams, the thickness, t, had to be uniform along the specimen length or in other words the ceramic layer should be parallel to the y axis (see Fig. 3(a)) to avoid torsion. It should be mentioned that in Eq. (1) the contribution from the adhesive is neglected as its thickness is relative small and its Young's modulus (approximately 2 GPa) is much lower than the Young's modulus of steel and the ceramic layer; the strain energy in the adhesive layers is thus diminishing small in comparison with the strain energy of the steel beams and the ceramic layer. In most cases the ceramic layer was not polished but in few cases one surface was polished with a diamond paste to 1 μm finish to facilitate observation of the two different phases, NiO and YSZ, respectively.

3.3. Applied energy-release rate

The DCB specimen loaded with pure bending moments (Fig. 4) is a steady-state specimen, as under constant moments, $\mathcal{G}$ is independent of the crack length as can be seen from Eq. (1).[20,28] Only measurement of the applied moment is necessary to calculate $\mathcal{G}$.

3.3.1. Loading arrangement and instrumentation

The pure bending moments are applied to the DCB specimen using a special fixture described in Ref. 17, 28 which can be operated inside the chamber of an environmental scanning electron microscope (ESEM) for *in situ* observation of the crack growth. In an ESEM the specimens need not to be coated with conductive layers as in a conventional SEM where the new surfaces created by crack growth "charge up" and cannot be observed in detail. All the tests were conducted at room temperature and at water vapour pressure of 50 Pa. The fixture was mounted on the XYZ stage of the microscope and thus by translating the stage in the specimen plane (XY) the crack growth increments (defined below) could be measured.

3.3.2. Loading procedure

Several measurements were performed on each specimen:

- First the DCB specimen was slowly loaded until a crack "popped in'" at the root of the micro-notch as shown in Fig. 6. The energy release rate at this first crack growth, from the blunted notch, is designated as $\mathcal{G}_{Ic}^*$. As soon as a crack initiated at the micro-notch, it grew continuously if $\mathcal{G}$ was
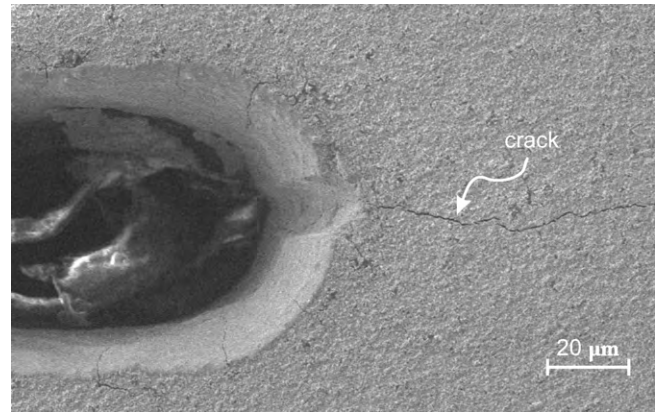

Fig. 6. Secondary-electron SEM micrographs of crack initiation.

not decreased since $\mathcal{G}_{Ic}^* > \mathcal{G}_{Ic}^i$ as mentioned in the previous section. Therefore, the specimen was partially unloaded (the applied $\mathcal{G}$ decreased around 30%) to arrest the crack after it had grown approximately 250 μm (five times the initial notch radius—see Fig. 7).

- Then (a) $\mathcal{G}$ was increased until the crack grew again, which corresponds to $\mathcal{G}_{Ic}^i$, and (b) followed by partial unloading ($\mathcal{G}$ was decreased about 8–10%). This procedure (the last two steps) was repeated eight times for each specimen.

- After the measurements of $\mathcal{G}_{Ic}^i$, the crack growth velocity as function of $\mathcal{G}$ was measured on the same specimen. The loading procedure was as following:

1. The applied $\mathcal{G}$ was increased rapidly (at a rate of ≈ 6 J/m^2/s) to a value larger than $\mathcal{G}_{Ic}^i$ for the specific specimen.
2. $\mathcal{G}$ was held constant for a time period Δt_i (typically 30 s).
3. The specimens was unloaded to $\mathcal{G} < \mathcal{G}_{Ic}^i$.
4. The applied $\mathcal{G}$ was held constant for a time period of ≈ 20 min.

During step 2 the crack grew (crack increment) a distance Δa_i. From these measurements it follows that the average crack growth velocity can be approximated as $v_i = \Delta a_i / \Delta t_i$. It should be noted that during crack growth (step 2) no significant decrease in applied $\mathcal{G}$ was observed (approximately 4% for applied energy-release rates close to $\mathcal{G}$ for fast fracture) and that
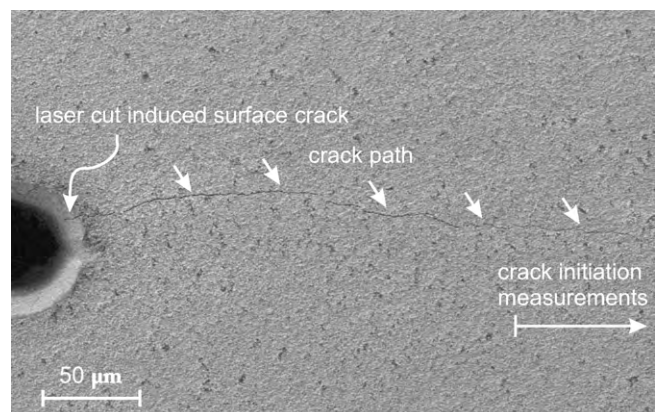

Fig. 7. Secondary-electron SEM micrograph of crack initiation.

at $\mathcal{G} < \mathcal{G}^i_{Ic}$ no crack growth took place. The applied $\mathcal{G}$ at step 4 corresponds to an applied energy release rate smaller than the applied energy release rate for crack arrest, $\mathcal{G}^a_{Ic}$. No effort was made to precise measure $\mathcal{G}^a_{Ic}$. A relatively large time period was selected for this step in order to ensure that indeed no very slow crack growth takes place at the applied $\mathcal{G}$ during this step. The estimated $\mathcal{G}^a_{Ic}$ value given in the next section is based on this time interval. The procedure described above was repeated several times (usually at $\mathcal{G}$ larger than at the previous step) until the case where the applied $\mathcal{G}$ caused fast fracture of the specimen. In this case the crack growth velocity was estimated by the remaining uncracked specimen length and time to failure.

4. Results and discussion

4.1. Critical energy-release rate for crack initiation (blunted notch), $\mathcal{G}^*_{Ic}$

The critical energy-release rate for the initiation of crack growth from the micro-notch is now presented. Fig. 6 depicts a crack initiated from the micro-notch. It is interesting to measure the critical energy-release rate from a notch and see how much it differs from the critical energy-release measured using a truly sharp crack. The measured values are given in Table 2. Note the low variability in the results, especially for a ceramic (brittle) material. As mentioned in a previous section, the main purpose of the micro-notch was to induce a sharp crack in the middle of the specimen—this is clearly shown in Fig. 6.

4.2. Critical energy-release rate for crack initiation (sharp crack), $\mathcal{G}^i_{Ic}$.

The measured values of the critical energy release rate associated with crack growth of a sharp crack tip are given in Table 3. Regarding the fracture energies (critical energy-release rates), it is observed, as expected, from Table 3 that they are lower than the corresponding values from a blunted notch (Table 2). Similarly to the previous observation (Table 2), the measurements appear to be very reproducible with only small differences from specimen to specimen.

Each row in Table 3 is the average of 8 crack growth measurements per specimen. The low value of the standard deviation for each specimen shows that the fracture energy does not vary

Table 2
Fracture energy and fracture toughness for crack initiation from micro-notch.

Specimen	$\mathcal{G}^*_{Ic}$ (plane stress) (J/m^2)	K^*_{Ic} (plane stress) (MPa$\sqrt{m}$)
1	32.2	2.23
2	31.7	2.22
3	31.2	2.20
4	31.7	2.22
5	35.8	2.36
6	24.6	1.95
7	29.5	2.14
Average	31.0	2.19
S.D.	3.4	0.12

Table 3
Fracture energy and fracture toughness for crack initiation from a sharp crack (8 measurements per specimen).

Specimen	$\mathcal{G}^i_{Ic}$ (plane stress) (J/m^2)		K^i_{Ic} (plane stress) (MPa$\sqrt{m}$)	
	Average	S.D.	Average	S.D.
1	25.1	2.0	1.97	0.09
2	22.7	1.2	1.87	0.05
3	23.7	0.5	1.90	0.02
4	20.8	1.1	1.80	0.05
5	30.0	1.1	2.16	0.05
6	26.4	1.2	2.02	0.05
7	28.0	1.3	2.08	0.05
Average	25.2		1.97	
S.D.	3.2		0.13	

significantly as the crack advances. Moreover, this variation was not monotonically increasing which suggests that the material does not possess *R*-curve behaviour. In addition no toughening mechanisms (*i.e.* crack bridging or surface uplift due to potential phase-transformation) were observed. The variation of the fracture energy values in each specimen could be attributed to local variations of porosity and grain sizes of the two phases.

Fig. 8 depicts backscatter electron micrographs of a polished specimen at two different applied $\mathcal{G}$. The use of a BSD detector
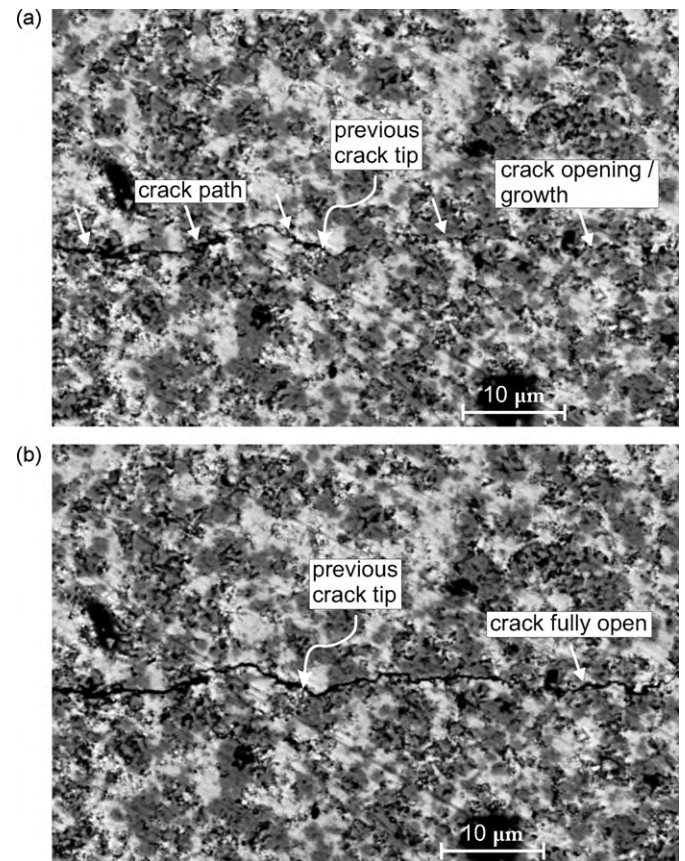

Fig. 8. Backscatter electron micrographs showing the crack opening and crack path with increasing applied $\mathcal{G}$. Darker gray is YSZ, lighter gray is NiO and black areas are porosity.
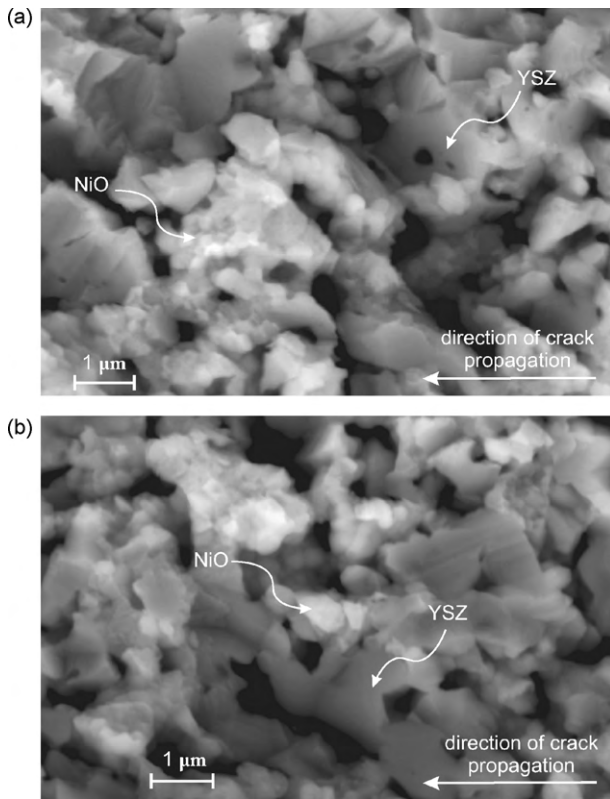
Fig. 9. Backscatter electron micrographs: cross-section view of fractured specimens.

enables the distinction of the two different phases in the material, NiO and YSZ, respectively. The crack path is strongly influenced by the grain sizes and distribution of the two phases. Next in Fig. 9 the cross-section of a fractured specimen is depicted. As it can be seen the YSZ phase is characterised by trans-granular fracture, whereas the NiO by inter-granular fracture. This failure mechanism was expected since the YSZ is the skeleton on which NiO particles are distributed.

Some further remarks on the results of Tables 2 and 3 are worth mentioning. The effect of the crack sharpness was theoretically analysed, using softening hyperelasticity, by Volokh and Trapper.[29] They concluded that the toughness can only be measured correctly if the crack sharpness is smaller than a characteristic length of the materials microstructure, *e.g.* the grain size. As mentioned above the notch radius was less 5–6 μm, whereas the estimated average grain size (see Fig. 8) is ≈3–5 μm. This can explain that the toughness measured by a sharp crack is only approximately 10% less than the toughness measured from the micro-notch. Kruzic et al.[27] found, for pyrolitic carbon materials, the fracture toughness from micronotched specimens (notch radius less than 5 μm) to be lower than the toughness measured in precracked specimens although by employing statistical approaches they showed that no significant difference exists between the two sets of measurements. Based on the experimental data presented here, the results of Kruzic et al.[27] and the analysis of Volokh and Trapper,[29] it can be argued that a notch radius less than grain size can be adequate for accurate toughness measurements.

4.3. Crack growth rate versus energy-release rate

It is common in brittle materials for the crack growth velocity to strongly depend on the applied $\mathcal{G}$.[11–13] This is also the case for the material tested in the present work as can be seen from Fig. 10, which depicts that crack-growth rate *versus* energy-release rate. The energy-release rate for fast fracture, $\mathcal{G}_{Ic}^f$, is 25–55% higher than the critical energy-release rate for crack initiation. The corresponding critical plane stress Mode I stress intensity factor for fast fracture, using Eq. (5), is $2.55 \pm 0.2 \, \text{MPa}\sqrt{m}$. The estimated value of $\mathcal{G} \le \mathcal{G}_{Ic}^a$ was 20.8 J/m² which is about 16% lower than the average value of $\mathcal{G}_{Ic}^i$. The implication of this phenomenon, as already mentioned in previous studies,[9] is that the measurement of critical energy-release rate based on fast fracture overestimate the toughness of the material. A safe design should be based on toughness value corresponding to crack arrest. It should be noted that in Fig. 10 the upper and lower crack growth velocities are approximate estimations.

An attempt is made here to compare the fracture toughness values of the current work with the limited data reported in literature. It should be mentioned, however, that direct comparison is not possible mainly due to differences in materials composition and processing parameters. Using the expression derived by Radovic and Lara-Curzio[6] the corresponding fracture toughness (fast fracture) for NiO–YSZ with 15% porosity is approximately $1.74 \, \text{MPa}\sqrt{m}$. In their work, the ZrO_2 was stabilised with 8 mol% Y_2O_3 in contrast to 3 mol% Y_2O_3 used in the present work. The difference in the Y_2O_3 content can explain that their fracture toughness value for fast fracture is significantly lower than the fracture toughness (fast fracture) reported in the present work ($2.55 \, \text{MPa}\sqrt{m}$) and it is even lower than the fracture toughness for crack initiation ($1.97 \, \text{MPa}\sqrt{m}$). Hbaieb,[7] using the controlled buckling test, measured the fracture toughness of NiO–YSZ, with composition very similar to our work, to be approximately $5.0 \, \text{MPa}\sqrt{m}$. This value is significantly higher than the values given in Table 3.
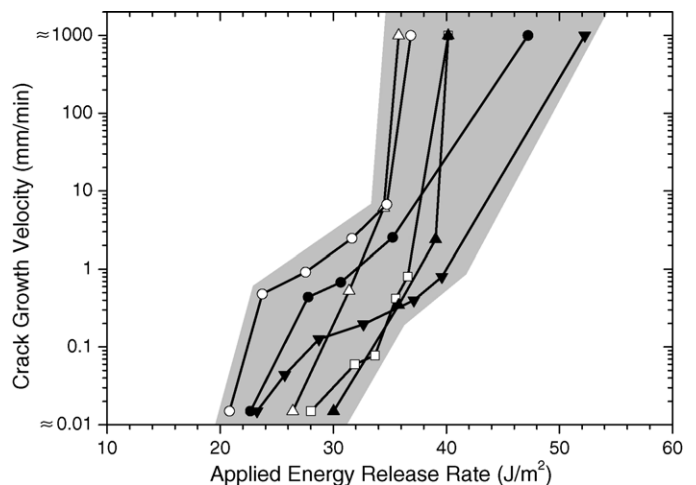

Fig. 10. Average crack growth rate as a function of applied $\mathcal{G}$.

As mentioned above, no phase-transformation (accompanied by volumetric dilation and shear) was observed as a result of crack propagation and thus R-curve behaviour (increase of fracture resistance with crack extension) due to transformation toughening was absent. Two reasons may be responsible for the lack of transformation toughening: (a) lack of constraint between the zirconia particles due to the presence of voids preventing autocatalysis,[30,31] and (b) the thermal history during processing resulted in a microstructure, *e.g.* particle size, that does not give tetragonal to monoclinic phase-transformation.[32,33]

5. Summary

A technique for evaluating the critical energy-release rate/fracture toughness of thin ceramic layers was described for anode materials used in fuel cells (NiO–YSZ). The approach involves a new specimen geometry, in which a thin layer is glued onto thicker steel beams. The advantages of the technique, stable crack growth combined with visual observation, allow a detailed description of the crack growth behaviour:

1. The fracture toughness for crack initiation from a sharp crack was measured with a very high reproducibility to be $1.97 \pm 0.13\,\mathrm{MPa}\sqrt{m}$.
2. It was demonstrated that the measurement of fracture toughness based on fast fracture can overestimate the fracture resistance from 25 to 55%.
3. It was shown that the main crack growth mechanisms are most likely (a) fracture along the interfaces of the different phases (with the presence of porous also to influence the crack path) and (b) trans-granular fracture of the YSZ phase.

References

1. Zhu WZ, Deevi SC. A review on the status of anode materials for solid oxide fuel cells. *Materials Science and Engineering* 2003;**A362**:228–39.
2. Atkinson A, Barnett S, Gorte RJ, Irvine JTS, Mcevoy AJ, Mogensen M, et al. Advanced anodes for high-temperature fuel cells. *Nature Materials* 2004;**3**:17–27.
3. Primdahl S, Mogensen M. Oxidation of hydrogen on ni/yttria-stabilized zirconia cermet anodes. *Journal of Electrochemical Society* 1997;**144**(10):3409–19.
4. Primdahl S, Mogensen M. Gas conversion impedance: a test genometry effect in characterization of solid oxide fuel cell anodes. *Journal of Electrochemical Society* 1998;**145**(7):2431–8.
5. Radovic M, Lara-Curzio E. Elastic properties of nickel-based anodes for solid oxide fuel cells as a function of the fraction of reduced NiO. *Journal of the American Ceramic Society* 2004;**87**(12):2242–6.
6. Radovic M, Lara-Curzio E. Mechanical properties of tape cast nickel-based anode materials for solid oxide fuel cells before and after reduction in hydrogen. *Acta Materialia* 2004;**52**:5747–56.
7. Hbaieb K. Measurement of fracture toughness of anode used in solid oxide fuel cell. *Thin Solid Films* 2009;**517**:4892–4.
8. Atkinson A, Selçuk A. Mechanical behaviour of ceramic oxygen ion-conducting membranes. *Solid State Ionics* 2000;**134**:59–66.
9. Kumar AN, Sørensen BF. Fracture resistance and stable crack-growth behavior of 8-mol%-ytria-stabilised zirconia. *Journal of the American Ceramic Society* 2000;**83**(5):1199–206.
10. Chen Z, Cotterell B, Wang W. The fracture of brittle thin films on compliant substrates in flexible displays. *Engineering Fracture Mechanics* 2002;**69**(5):597–603.
11. Wiederhorn SM. Influence of water vapor on crack propagation in soda-lime glass. *Journal of the American Ceramic Society* 1967;**50**(8):407–14.
12. Evans AG. A method for evaluating the time dependent failure characteristics of brittle materials—and its application to polycrystalline alumina. *Journal of Materials Science* 1972;**7**:1137–46.
13. Freiman SW, Mulville DR, Mast PW. Crack propagation studies in brittle materials. *Journal of Materials Science* 1973;**8**:1527–33.
14. Nishida T, Hanaki Y, Pezzotti G. Effect of notch root radius on the fracture toughness of a fine-grained alumina. *Journal of the American Ceramic Society* 1994;**77**(2):606–8.
15. Damani R, Gstrein R, Danzer R. Critical notch-root radius effect in SENB-S fracture toughness testing. *Journal of The European Ceramic Society* 1996;**16**:695–702.
16. Sherman D. Fracture toughness evaluation of small thin ceramic specimens. *Journal of the American Ceramic Society* 1997;**80**(7):1904–6.
17. Sørensen BF, Horsewell A, Jøgensen O, Kumar AN, Engbæk P. Fracture resistance measurement method for in situ observation of crack mechanisms. *Journal of the American Ceramic Society* 1998;**81**(3):661–9.
18. Rice JR. A path independent integral and the approximate analysis of strain concentrations by notches and cracks. *Journal of Applied Mechanics* 1968;**35**:379–86.
19. Bao G, Ho S, Suo Z. The role of material orthotropy in fracture specimens for composites. *International Journal of Solids and Structures* 1992;**29**(9):1105–16.
20. Hutchinson JW, Suo Z. Mixed-mode cracking in layered materials. *Advances in Applied Mechanics* 1992;**29**:63–191.
21. ASTM:E399–90. Plane-strain fracture toughness of metallic materials. West Conshohocken, PA, USA: American Society for Testing and Materials; 1997.
22. Chantikul P, Anstis GR, Lawn BR, Marshall DB. Critical evaluation of indentation techniques for measuring fracture toughness: Ii, strength method. *Journal of the American Ceramic Society* 1981;**64**(9):539–43.
23. Nose T, Fujii T. Evaluation of fracture toughness for ceramic materials by a single-edge-precracked-beam method. *Journal of the American Ceramic Society* 1988;**71**(5):328–33.
24. Pancheri P, Bosetti P, Maschio RD, Sglavo VM. Production of sharp cracks in ceramic materials by three-point bending of sandwiched specimens. *Engineering Fracture Mechanics* 1998;**59**(4):447–56.
25. Carpenter RD, Paulino GH, Munir ZA, Gibeling JC. A novel technique to generate sharp cracks in metallic/ceramic functionally graded materials by reverse 4-point bending. *Scripta Materialla* 2000;**43**:547–52.
26. Hashimoto A, Kovar D. Controlled precracking of fracture mechanics specimens using contact stresses. *Journal of the American Ceramic Society* 2002;**85**(9):2251–5.
27. Kruzic JJ, Kuskowski J, Ritchie RO. Simple and accurate fracture toughness testing methods for pyrolytic carbon/graphite composites used in heart-valve prostheses. *Journal of Biomedical Materials Research Part A* 2005;**74A**(3):461–4.
28. Sørensen BF, Brethe P, Skov-Hansen P. Controlled crack growth in ceramics: the DCB specimen loaded with pure moments. *Journal of the European Ceramic Society* 1996;**16**:1021–5.
29. Volokh KY, Trapper P. Fracture toughness from the standpoint of softening hyperelasticity. *Journal of the Mechanics and Physics of Solids* 2008;**56**:2459–72.
30. Stump DM. The role of shear stresses and shear strains in transformation-toughening. *Philosophical Magazine A* 1991;**64**(4):879–902.
31. Stump DM. Autocatalysis: the self-induced growth of martensitic phase transformations in ceramics. *Acta Metallurgica Materialia* 1994;**42**(9):3027–33.
32. Evans AG, Cannon RM. Toughening of brittle solids by martensitic transformations. *Acta Metallurgica* 1986;**34**(5):761–800.
33. Hannink RHJ, Garvie RC. Sub-eutectoid aged Mg–PSZ alloy with enhanced thermal up-shock resistance. *Journal of Materials Science* 1982;**17**:2637–43.